Nonlinear dynamics in periodically repeated sets of directional solidification cells

Mark J. Bennett, Konstantinos Tsiveriotis, and Robert A. Brown

Department of Chemical Engineering, Massachusetts Institute of Technology, Cambridge, Massachusetts 02139
(Received 7 October 1991)

Numerical simulations of two-dimensional, spatially periodic cellular structures in directional solidification of a binary alloy show the existence of multiple steady-state, traveling-wave, and spatiotemporally chaotic structures in samples that admit up to eight cells. This variety of dynamics is observed within a small range of dimensionless growth rate P above the critical value P_c and transitions occur on long time scales; both phenomena are linked to the shallow neutral stability curve, which controls the initial formation of cells. Traveling-wave states bifurcate supercritically from stationary cellular patterns and have lateral wave speeds that increase proportional to $P - P_c$, in agreement with the theory for traveling waves introduced by parity-breaking bifurcations.

I. INTRODUCTION

As the question of wavelength selection in the microstructures formed in two-dimensional directional solidification experiments receives more attention, it is becoming increasingly clear that the cellular patterns observed do not exhibit a unique relationship between growth rate and wavelength, but that a myriad of structures along the interface are possible, representing a band of length scales in the solidification microstructure. Moreover, the selection of particular states within this band is influenced by nonlinear dynamical phenomena caused by interactions between neighboring cells. This paper reports numerical simulations for the evolution of a section of a laterally periodic solidification interface, as a mechanism for probing the nonlinear dynamics of cellular structures and the microstructural length scales of the interface.

Cellular structures in directional solidification form along the melt-solid interface of a binary alloy as the growth rate is increased for a constant temperature gradient. A planar interface initially becomes unstable to sinusoidal disturbances of infinitesimal amplitude.[1] The relationship between the wavelength of the undulation λ and the growth rate V at which the instability begins is given by the neutral stability relation $V = V(\lambda)$ from linear stability theory.[1] The critical growth rate $V \equiv V_c$ is the lowest value for neutral stability and occurs at the most dangerous wavelength $\lambda \equiv \lambda_c$. As is typical in nonlinear transport processes involving diffusion, the neutral stability curve is locally parabolic about $\lambda \equiv \lambda_c$. For $V > V_c$, linear stability theory predicts that the planar front is unstable to a band of wavelengths. The problem of wavelength selection for finite amplitude cells focuses on understanding the evolution of the solidification interface in this state. The analysis for cellular solidification is particularly complex because the typical neutral stability curve is extremely flat; that is, for V slightly above V_c, a large band of wavelengths is unstable. Bifurcation analysis applied to small collections of cells has shown that this flatness leads to nonlinear interactions between

cells with spatially resonant wavelengths at growth rates very close to V_c.[2-4]

We believe that the presence of these nonlinearly coupled modes causes temporal interactions along a cellular front and leads to time-dependent dynamics. This view has been partially substantiated by the time-dependent simulations of cellular growth of Bennett and Brown,[5] who demonstrated that time-periodic and aperiodic states were possible for a collection of shallow, two-dimensional cells confined between rigid boundaries as V was increased. In these simulations, the microstructure changed continuously in time over a scale of 100–1000 diffusion times, based on the cell size. A unique cellular pattern was not observed for V above a threshold extremely close to V_c and the "average wavelength" of the cellular structure decreased with increasing growth rate.

The time-dependent dynamics in these simulations seemed to result from interactions of the birth and death of individual cells along the front with adjustments in the wavelength and phase of the front caused by the lateral motion of irregularities in the front—traveling waves. Cell birth is by tip splitting and is connected to the codimension-2 bifurcations caused by spatial resonance of cells with wavelength λ and $\lambda/2$; see Refs. 2–6 for a description of this phenomenon. The local birth of a new cell causes an asymmetry in the spatial periodicity of the front and leads to lateral migration of the cell. During this migration and in subsequent dynamics, the new cell formed by the splitting may persist or be consumed by its nearest neighbors. In the simulations of Bennett and Brown (Ref. 5, henceforth referred to as BB), the sample was surrounded by rigid boundaries where reflective symmetry was imposed on the field variables and the interface. Hence, traveling waves in the interface structure were reflected back from the boundaries. The aperiodic dynamics observed with increasing growth rate is caused, at least partially, by the interactions of traveling-wave states moving in both directions.

These predictions from simulations are very difficult to confirm experimentally because of the very narrow range of growth rate over which the transitions occur; however,

several recent directional solidification experiments do bear on these predictions. Two-dimensional directional solidification experiments of an organic alloy by Lee[6] focus on observation of the development of the cellular pattern near onset $(V = V_c)$ over a long time. These experiments show the evolution of the interface structure to wavelengths less than λ_c and demonstrate aperiodic dynamics over long time scales involving cell wavelengths within a band. The dynamics of the front is marked by tip splitting and lateral motion of cells over short distances; however, true traveling waves have not been seen. Overall, the interface appears to be undergoing a form of spatiotemporal chaos that is similar to states observed in other systems with large aspect ratios[8-10] and to observations reported by others in directional solidification.[11-13]

Most notable among these are directional solidification experiments of Simon, Bechhoefer, and Libchaber[11] for the thermal transition between isotropic and nematic liquid-crystalline phases in a thin-film experiment. Again there is a critical velocity for the onset of a cellular pattern. For a range of velocities above this value, the interface has a broad band of wavelengths, similar to the spectrum seen in Ref. 6; however, above a second critical value, solutions in the form of traveling waves are observed. With the presence of these solitary waves, the band shifted to lower wavelengths and narrowed considerably.

The experiments of Cladis, Gleason, and Finn[12,13] for thin-film directional solidification of an organic alloy also substantiate the picture introduced by BB of spatiotemporal chaos in this system. Two additional critical growth rates (V_{c1}, V_{c2}) were observed in these experiments: for $V_c < V < V_{c1}$ and $V > V_{c2}$, spatiotemporal chaos is observed. In the interval $V_{c1} < V < V_{c2}$, lateral propagation of the interface is observed and wavelength selection is enhanced considerably.

Spatiotemporal chaos and traveling waves have also been observed in the directional viscous fingering experiments of Rabaud, Michalland, and Couder.[10] The physics of these systems, caused by the balancing of viscous and surface-tension forces leads to a much stronger dependence of the critical velocity on the cellular wavelength and much more regular interfacial patterns.[14]

Coullet, Goldstein, and Gunaratne[15] advanced a model for the cause of traveling-wave solutions in nonlinear transport problems with spatially periodic structures. The model is based on the idea of a disturbance that breaks the natural parity of the reflectively symmetric cells and leads to anisotropy in the structure to traveling-wave solutions. Coullet, Goldstein, and Gunaratne, and, later Goldstein et al.,[16] used multiple length scale analysis to derive generic amplitude equations describing the onset of a parity-breaking instability to an initially cellular state. The results of this analysis suggest that traveling-wave solutions exist beyond a critical value of the control parameter and that the wave speed is proportional to the difference $(V - V_c)$. The calculations described in Sec. III confirm this prediction. Proctor and Jones[17] have explained the existence of traveling-wave solutions due to the presence of codimension-2 bifurcation points. Levine and Rappel[18]

applied the results of Proctor and Jones to the system of directional solidification and compared with calculations of traveling waves for conditions meant to correspond to the liquid-crystal system used in Ref. 11. Again, the flatness of the neutral stability curve makes these states accessible at conditions only slightly above critical.

II. MODEL FORMULATION AND SOLUTION METHOD

A. Solutal model

The numerical simulations described here are based on analysis of the solutal model of alloy solidification described in BB. Here the melt and solid are modeled as having equal thermal conductivities; latent heat release at the melt-crystal interface and convective heat transport are ignored. With these assumptions, a constant temperature gradient G imposed in the direction of crystal growth is unaltered by the shape of the melt-crystal interface, which is computed from analysis of the solute field and from the Gibbs-Thomson condition for interfacial equilibrium. Dimensionless model equations are obtained by scaling lengths with the characteristic wavelength λ_0 of a cell, temperatures with the melting temperature of the pure material T^0, concentrations with the bulk concentration of the melt c_0, and time with the diffusive scale $\lambda_0^2/\mathcal{D}$. The dimensionless solute balances are

$$\nabla^2 c_m + P\frac{\partial c_m}{\partial y} = \frac{\partial c_m}{\partial \tau} \tag{1}$$

in the melt and

$$R_m \nabla^2 c_s + P\frac{\partial c_s}{\partial y} = \frac{\partial c_s}{\partial \tau} \tag{2}$$

in the solid, where y is the coordinate direction for growth, τ is the dimensionless time, $R_m \equiv \mathcal{D}_s/\mathcal{D}_m$ is the ratio of the solute diffusivities in the solid and melt, and $P \equiv V\lambda_0/\mathcal{D}_m$ is the Péclet number of dimensionless translation rate of the sample.

At the interface, the concentration of solute in the solid c_s and melt c_m are related by the idealized phase relation $c_s = kc_m$, where k is the segregation coefficient, and by the interface solute balance

$$(\hat{n}\cdot\nabla c_m) + R_m(\hat{n}\cdot\nabla c_s) = (\hat{n}\cdot\hat{e}_y)[P + V_e(x,t)](k-1)c_m , \tag{3}$$

where $V_e(x,t)$ is the vertical component of the interface velocity in the y direction in excess of P, $\hat{e}_y$ is the unit vector in the y direction, and $\hat{n}$ is the unit normal vector to the interface pointing into the melt. The Gibbs-Thomson condition for interfacial equilibrium is written as

$$c_{\text{ref}} + \frac{Gy}{m} = c_m + \frac{\Gamma}{m}2\mathcal{H} , \tag{4}$$

where $\mathcal{H}$ is the mean curvature of the interface, m is the slope of the liquidus curve, Γ is the dimensionless capillary length, G is the dimensionless temperature gradient, and c_{ref} is a reference concentration that is fixed at the

concentration in the melt for a planar interface; $c_{ref} = 1/k$. The definitions of the dimensionless groups used here are the same as reported in Table II in BB. The dimensionless translation rate P is used as the parameter for initiating and increasing the amplitude of the cells.

The values of the dimensionless groups used in the calculations are $k = 0.1$, $R_m = 1.0$, $G = 2.1 \times 10^{-3}$, $m = -6.7 \times 10^{-4}$, and $\Gamma = 1.6 \times 10^{-7}$. The neutral stability curve from linear stability theory for these parameters is shown as Fig. 1 in BB.

B. Numerical method

We compute time-dependent solutions to the solutal model with the conditions that the concentration field and the interface shape are spatially periodic for an interval of the interface $0 \leq x \leq L$. The numerical integration is conducted using the finite-element–isotherm method described by Ungar, Ramprasad, and Brown.[19] Galerkin finite element discretization is used to reduce the continuous problem to a set of differential-algebraic equations (DAE's), which are integrated using a fully implicit, second-order accurate Adams-Moulton method: see Ref. 19 for details. The calculations presented here are for L taken to be an integer number, i.e., for sample sizes that admit the development of an integer number of small amplitude cells from the planar state. The problem is discretized by using 16 finite elements along the interface for each primary wavelength and ten elements in each the melt and solid. The total number of DAE's solved ranged from 1024 for $L = \lambda$ to 8192 for $L = 8\lambda$, where λ is the nominal wavelength of the cells; only $\lambda = \lambda_c$ will be considered here. See Bennett[20] for details.

C. Neutral stability and symmetry considerations

Introducing boundary conditions for spatial periodicity alters the steady state solutions computed in BB for the same conditions, by eliminating solutions that do not have periodic structure. With reflective symmetry conditions, a collection of n cells with wavelength λ computed in the L-sized box need only satisfy the relation $n(\lambda/2) = L$ to be admissible; i.e., an integer number of half wavelengths must fit into the sample. For a spatially periodic domain the cells must satisfy $n\lambda = L$, so that an integer number of wavelengths must fit into the sample. This added restriction in the periodic sample increases the size of the sample needed to see many of the steady-state and time-periodic forms computed in BB. For example, the steady-state family of cells with wavelength λ is computed in a sample of size $L = \lambda/2$ if reflective conditions are used, but requires a sample size of $L = \lambda$ with periodic conditions.

The primary bifurcation points for periodic sample sizes with $L = 1$, 2, 4, and 8 times the critical wavelength λ_c are listed in Table I for a narrow range of growth rates and Péclet numbers. Besides integer multiples of cells with wavelength λ_c, forms with smaller numbers of larger cells and with large numbers of smaller cells are admissible. Most importantly, the time-dependent dynamics involving tip splitting and traveling waves that is reported in BB requires $L = 2\lambda_c$ for reflective conditions; hence, this dynamics is expected in samples larger than $L = 4\lambda_c$ for the periodic boundary conditions.

The steady-state, tusk-shaped shapes discovered by BB for $L = 2\lambda_c$ satisfy the reflective boundary conditions by coming in pairs with the shapes either tilted inward or outward. These shapes are not allowed with periodic boundary conditions; however, shapes that all tilt in either the positive or negative x direction are admissible. Fronts of such tilted cells cause a skew in the concentration field and lead to lateral motion of the cells, i.e., traveling waves, as observed in experiments[11] and calculations.[18]

III. SIMULATION RESULTS

Time-dependent simulations were carried out for varying Péclet number P and for sample sizes in the interval

TABLE I. Primary bifurcation points for the shape families admissible in periodic domains with widths of four different sizes: $L = \lambda_c$, $2\lambda_c$, $4\lambda_c$, and $8\lambda_c$.

	Families for periodic samples					
$1\lambda_c$	$2\lambda_c$	$4\lambda_c$	$8\lambda_c$	$P \; (\equiv V\lambda_{ref}/\mathcal{D})$	$\epsilon \; [\equiv 100(P - P_C)/P_C]$	$V \; (\mu m/s)$
1				0.39141	0.0000	4.2324
			8/9	0.39146	0.0128	4.2329
			8/7	0.39147	0.0153	4.2330
		4/5		0.39160	0.0485	4.2345
		4/3		0.39169	0.0715	4.2354
			8/11	0.39182	0.1047	4.2368
	2/3			0.39210	0.1763	4.2398
			8/5	0.39213	0.1840	4.2402
			8/13	0.39244	0.2632	4.2435
		4/7		0.39283	0.3628	4.2478
	2			0.39296	0.3960	4.2492
			8/15	0.39328	0.4778	4.2526
1/2				0.39377	0.6029	4.2579

$\lambda_c \leq L \leq 8\lambda_c$. These results are reported separately for each sample size.

A. The $L = \lambda_c$ sample

This sample is important as a base case for the interactions between the wavelengths λ_c and $\lambda_c/2$. As shown in Table I only cell shapes with wavelengths λ_c and $\lambda_c/2$ bifurcate for $L = \lambda_c$ in the parameter range $0.3914 \leq P \leq 0.407$. As expected from the analyses of Haug[7] and Proctor and Jones,[17] quadratic nonlinearities will lead to interactions between the spatial modes involving the wavelengths λ_c and $\lambda_c/2$. Such interactions lead to a number of characteristic types of steady and transient nonlinear behavior: (i) the steady $1\lambda_c$ solution joins the steady $1/2\lambda_c$ solution at a secondary bifurcation, (ii) a Hopf point is possible on the $1\lambda_c$ solution leading to standing waves, and (iii) a traveling wave solution bifurcates from the $1\lambda_c$ family for periodic boundary conditions. The connectivity between the steady primary solutions $1/\lambda_c$ and $2\lambda_c$ and the Hopf point on the $1\lambda_c$ family have been studied numerically[2,5] and analytically.[7,17] Here we concentrate on the traveling-wave solution.

Time integration reveals a supercritical transition from the steady one-cell solution to a traveling wave at $P_t = 0.393\,05$; we refer to this state as $1\lambda_c$ TW, since its spatial period is λ_c. For $P < P_t$, the steady $1\lambda_c$ family is stable, while for $P > P_t$ stable traveling waves are predicted; calculations were performed up to $P = 0.3940$, as shown in Fig. 1. Both these states involve mainly two spatial modes with wavelengths λ_c and $\lambda_c/2$, but in the traveling wave these modes are out of phase. Here a phase difference is defined as

$$\chi \equiv 2 \left[\theta + 2\pi \frac{x}{\lambda_c} \right] - \left[\phi + 2\pi \frac{x}{\lambda_c/2} \right] = 2\theta - \phi , \qquad (5)$$

where $[\theta + 2\pi(x/\lambda_c)]$ and $\{\phi + 2\pi[x/(\lambda_c/2)]\}$ are the phases of the λ_c and $\lambda_c/2$ modes, respectively. The phase difference χ is plotted as a function of the dimensionless growth velocity P in Fig. 2. As shown there, for

FIG. 2. Phase shift between the two leading modes in steady- and traveling-wave solutions for $L = \lambda_c$.

$P > P_t$, the phase difference χ deviates from π resulting in asymmetric cellular shapes and concentration fields. This asymmetry causes the lateral migration of the cells with traveling speed that increases as the phase difference $|\chi - \pi|$ increases, as shown in Fig. 3, in agreement with the predictions of Coullet, Goldstein, and Gunaratne[15] and Proctor and Jones.[17] For the shape of the traveling wave shown in Fig. 1 the traveling velocity is pointing towards increasing values of the x coordinate; the reflection of this wave also is a solution traveling towards decreasing values of x.

The quantity χ is not new but has been used in the past[17] to account for periodic boundary conditions in the interactions of the two spatial modes $e^{(i2\pi x/\lambda)}$ and $e^{(i4\pi x/\lambda)}$ involved in a codimension two singularity with 1:2 spatial resonance. In contrast to the case of reflective boundary conditions where the amplitudes of the two critical modes $e^{(i2\pi x/\lambda)}$ and $e^{(i4\pi x/\lambda)}$ are enough to describe the center manifold of the singularity, in the case of periodic boundary conditions both the amplitudes and the phase χ are needed, resulting in a three dimensional dynamical system.[17] An important result of the asymptotic analysis of Ref. 17 was that the amplitudes of the two
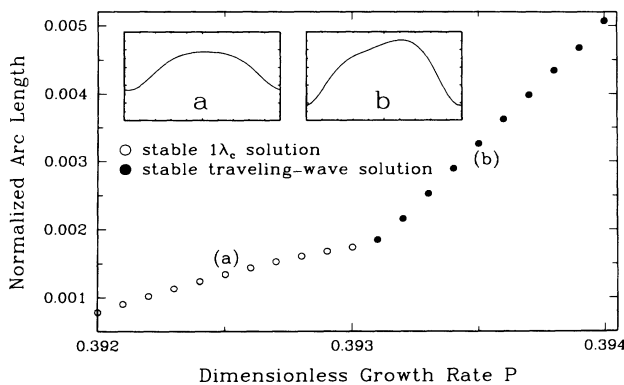

FIG. 1. Results from time integration in the $L = \lambda_c$ domain with periodic boundary conditions. Sample interface shapes for the steady- and traveling-wave solutions are also shown.
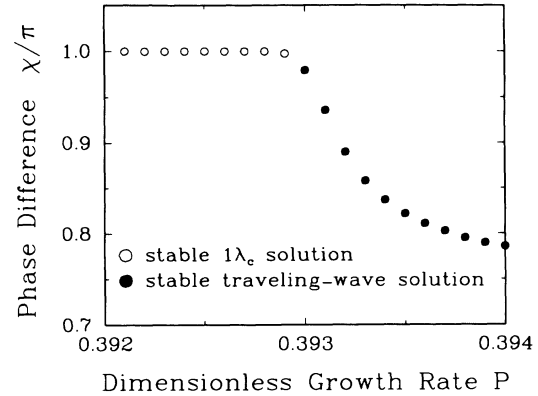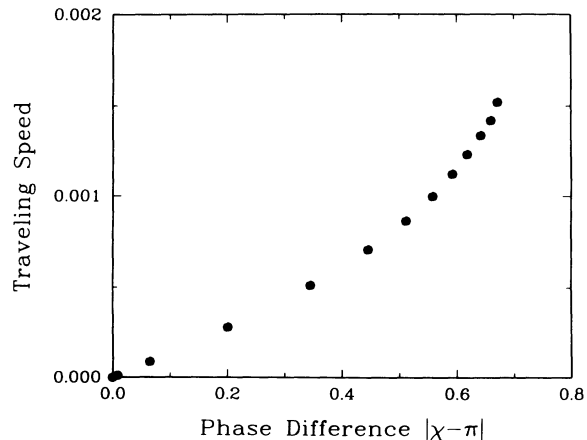

FIG. 3. Traveling velocity as a function of phase shift χ for the traveling-wave state of $L = \lambda_c$.
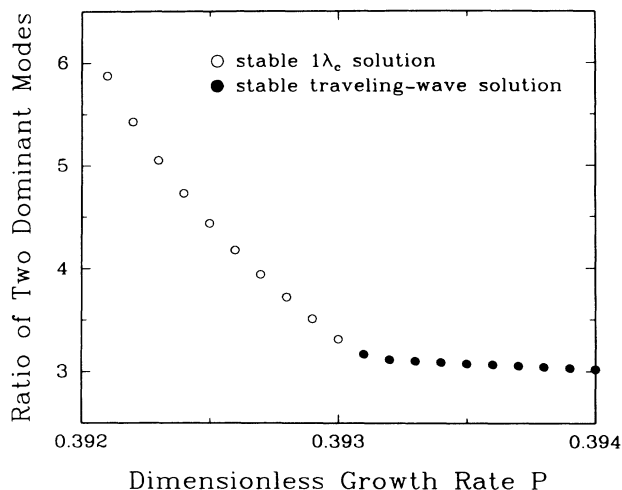
FIG. 4. Ratio of the amplitudes of the two spatial modes with wavelengths λ_c and $\lambda_c/2$ for the steady- and traveling-wave solutions in $L = \lambda_c$.
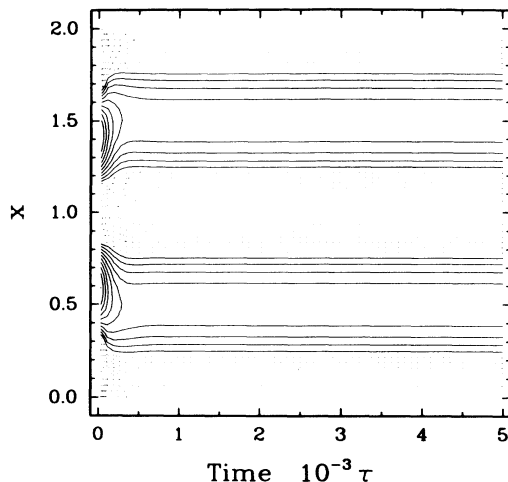

FIG. 5. Contours of the melt- solid interface height for simulation with $P = 0.3920$ and $L = 2\lambda_c$. Solid contours represent the portion of the interface above the average height and dotted contours represent points below this level.

dominant spatial components of the traveling wave have constant ratio. This is demonstrated by the calculations shown in Fig. 4.

The traveling-wave state described in this subsection is the simplest and best studied dynamical behavior differentiating the solidification system with periodic boundary conditions from that with reflective boundary conditions. New and more complex states appear as the length of the domain increases admitting an increasing number of spatial modes.

B. The $L = 2\lambda_c$ sample

As shown in Table I, increasing the sample size to $L = 2\lambda_c$ leads to the possibility of nonlinear interactions

with modes of wavelength λ_c, $2\lambda_c$, $2/3\lambda_c$, and $\lambda_c/2$. Dynamical simulations were performed for the values of P listed in Table II. Four qualitatively different types of behavior were found and are in sharp contrast to the dynamics seen in BB for samples with $L = 2\lambda_c$ and reflectively symmetric boundaries. The initial conditions for each of these simulations and the final states reached are discussed below.

1. Steady- and standing-wave states

First, the simulation for $P = 0.3920$ produced a steady-state structure with two cells of wavelength λ_c; the transient lasted approximately $\Delta\tau = 400$ and the steady-state shape persisted for $\Delta\tau = 5000$ units, corresponding to 15 h of growth. The contours of the inter-
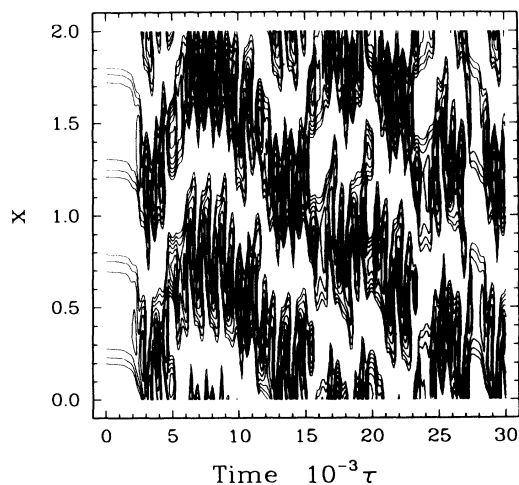
TABLE II. Growth rate and results for simulations in sample with $L = 2\lambda_c$.

Dimensionless growth rate P	Dynamic behavior
0.392 000	Stable steady-state growth with λ_c cells
0.393 215	Weakly aperiodic dynamics
0.393 000	Periodic dynamics showing height oscillation, tip splitting, and lateral shifts of cells
0.393 100	Periodic dynamics showing tip splitting and cell annihilation
> 0.393 200	Traveling-wave solutions

FIG. 6. Contours of interface amplitude computed at $P = 0.392\,15$ and $L = 2\lambda_c$. Only contours corresponding to the portion of the interface above the average height are shown.

face shape for this state are shown in Fig. 5 as a function of time τ. The initial condition for this simulation was the time periodic state found by BB for $P=0.3930$ with reflective boundary conditions. The same initial condition was also tried for $P=0.3930$ and periodic boundary conditions giving distinctly different behavior than that seen by BB, as discussed later in this section.

Starting a transient simulation with an initial condition composed of tusk-shaped cells from a calculation with reflective boundary conditions produced interface dynamics that is very different from what is described above. This is demonstrated using an initial condition composed of two outside facing tusks computed in a sample with $L=2\lambda_c$ and reflectively symmetric boundary conditions. With only a very slight increase in the
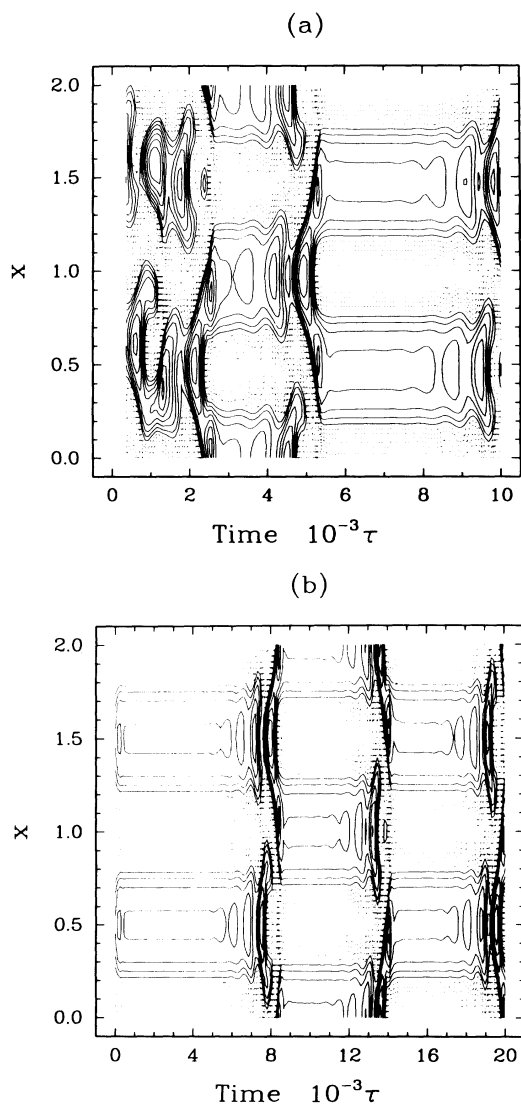
(a)

(b)

FIG. 7. Contours of interface amplitude computed in simulations for $P=0.3930$ and $L=2\lambda_c$ and $L=2\lambda_c$ for two different initial conditions: the initial states are (a) the time-periodic state described in BB for $P=0.3932$ and reflective boundary conditions and (b) the solution from the simulation with $P=0.3920$ at $\tau=5000$.

growth rate to $P=0.393\,215$ the cellular front continued to evolve in time for $\Delta\tau=30\,000$ in what appeared to be an aperiodic trajectory. The lack of temporal periodicity is demonstrated by the contours of the interface height shown in Fig. 6. Although the dynamics appears exceedingly complicated, the local behavior of the interface is characterized by only a few types of generic behavior. At short times the heights of the two tusks in the initial state begin to oscillate out of phase with one another. These oscillations increase in amplitude until tip splitting of one cell occurs and a small cell moves laterally into the neighboring groove and is dissolved. This sequence is repeated throughout the simulation with both cells showing tip splitting, cell migration, and dissolution, and is qualitatively similar to experimental observations discussed in Sec. I.

Simulations for $P=0.3930$ exhibited dynamics with tip splitting for two distinctly different initial conditions. In the first, the initial condition was the same as the one described for the simulation with $P=0.3920$. The results for the calculation with $P=0.3930$ are shown in Fig. 7(a). After an initial transient of approximately $\Delta\tau=2000$, the tip of the cell with its center at $x\approx0.5$ splits and both cells persist at the expense of the cell with center at $x\approx1.5$. As a result, the centers of the cells are shifted approximately $\Delta x\approx0.5$, or one half of a cellular wavelength. The newly developed cells are almost stable, except for slight amplitude oscillations, which grow in magnitude for $\Delta\tau=2000$ until tip splitting occurs again and the cycle is repeated.

The same behavior, amplitude oscillation, followed by tip splitting and cell death also was observed in a simulation for $P=0.3930$ using the solution from the simulation with $P=0.3920$ at $\tau=5000$ as an initial condition. The contours of interface amplitude computed in this simulation are shown in Fig. 7(b). The periodic dynamics of the interface is clearest from Fig. 8, where the arc length
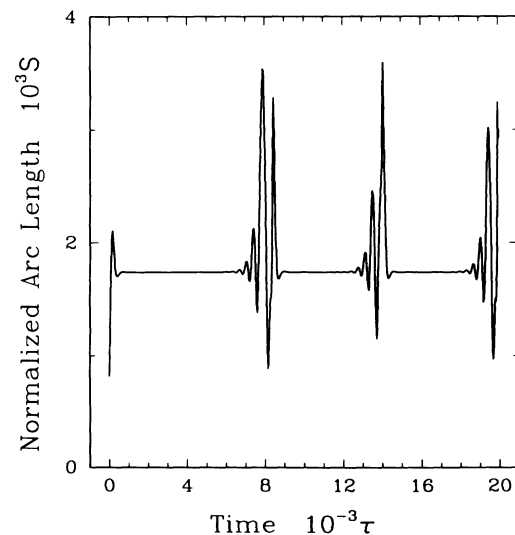
FIG. 8. Plot of the normalized arc length $S=S(\tau)$ along the interface for the simulation described in Fig. 7(b).

along the interface $S = S(\tau)$ normalized with the value for the planar state is plotted; see BB for a precise definition of S. In this projection the oscillation appears to have intermittent or bursting character.

Another standing-wave state was obtained for $P = 0.3931$ using a new traveling wave as the initial condition, as described in the following subsection.

2. Traveling-wave states

First, simulations with dimensionless growth rates in the range $0.3932 \leq P \leq 0.3942$ were carried out to examine whether the traveling-wave state $1\lambda_c$ TW found for $L = \lambda_c$ is stable for $L = 2\lambda_c$. The traveling wave solutions for $L = \lambda_c$ repeated twice in the x direction were used as initial conditions for the various values of the growth rates. These simulations verified that the $1\lambda_c$ TW state exists for $0.3932 \leq P \leq 0.3942$ in the $L = 2\lambda_c$ domain, as shown in Figs. 9(a) and 10.

Trying a different initial condition revealed a second family of traveling solutions, shown in Figs. 9(b) and 10. The initial condition used was the steady-state solution of two cells with wavelength λ_c computed at $P = 0.3920$. After an initial transient of $\Delta\tau \approx 1500$ the interface settled into two tusk-shaped cells that pointed to and traveled laterally in the negative x direction at a dimensionless speed of $V_t \approx 1.0 \times 10^{-3}$ (0.01 μm/s) or two orders of magnitude slower than the dimensionless growth rate $P = 0.3935$. The contours of the interface amplitude for this simulation are shown in Fig. 11. Although the traveling wave appears to move at constant velocity after the
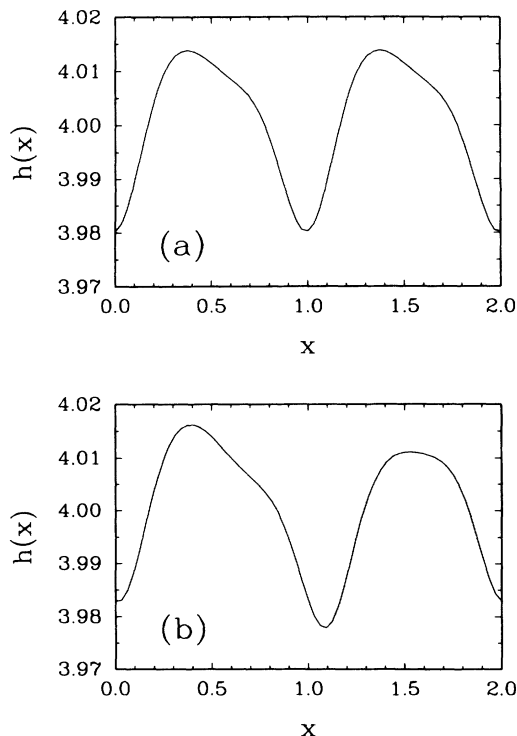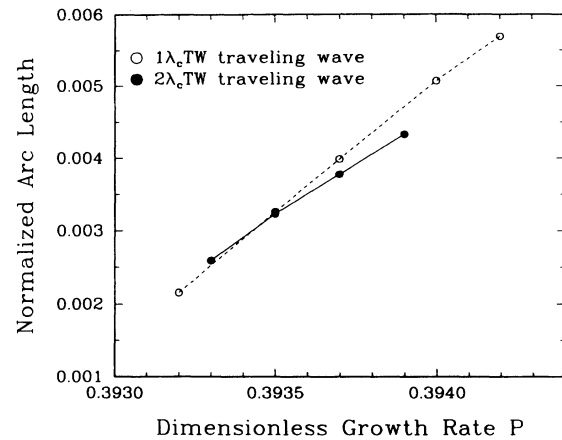

FIG. 10. Traveling-wave states for $L = 2\lambda_c$.

initial transient $(\tau > 1500)$, there are subtle changes in the wave shape at longer times. For times between $2000 < \tau < 4200$, the interface is composed of two, almost identical tusk-shaped cells. However, at longer times there is a shift to a pair of cells in which only one is tusk-like and the other is a slightly distorted cell with wavelength slightly less than λ_c as shown in Fig. 9(b); we refer to this traveling-wave state as the $2\lambda_c$ TW state because its spatial period is $2\lambda_c$. With the result of this simulation as the initial condition simulations were performed for dimensionless growth rates of 0.3931, 0.3933, 0.3935, 0.3937, 0.3939, and 0.3940, as shown in Fig. 10. The $2\lambda_c$ TW state existed for dimensionless growth rates $0.3933 \geq P \geq 0.3940$. For $P = 0.3942$, the $2\lambda_c$ TW state became unstable and the interface evolved to the $1\lambda_c$ TW state after approximately 4000 time units. On the other hand, for $P = 0.3931$, the $2\lambda_c$ TW state ceased to exist and periodic dynamics resulted involving tip splitting and
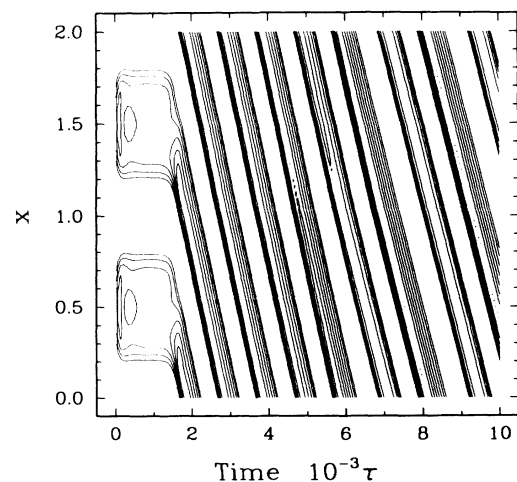

FIG. 9. Traveling-wave state at $P = 0.3935$, (a) $1\lambda_c$ TW family and (b) $2\lambda_c$ TW family.

FIG. 11. Contours of interface amplitude for $P = 0.3935$ and $L = 2\lambda_c$.

TABLE III. Stable steady-state solutions for $L = 4\lambda_c$.

Dimensionless growth rate P	Initial condition	Approximate wavelength of steady-state cells
0.393 215	(a) Outside facing tusks	$\frac{4}{5}\lambda_c$
	(b) Solution for $P = 0.393\,215$ and $\tau = 3 \times 10^4$ for $L = 2\lambda_c$	
0.393 300	Solution for $P = 0.393\,215$ and $\tau = 3 \times 10^4$ for $L = 2\lambda_c$	$\frac{4}{5}\lambda_c$
0.393 400	Solution for $P = 0.393\,215$ and $\tau = 3 \times 10^4$ for $L = 2\lambda_c$	$\frac{4}{5}\lambda_c$
0.393 500	Outside facing tusks	$\frac{4}{5}\lambda_c$
0.394 000	Solution for $P = 0.393\,215$ and $\tau = 3 \times 10^4$ for $L = 2\lambda_c$	$\frac{2}{3}\lambda_c$

cell annihilation to a neighboring grove, as shown in Fig. 12.

C. The $L = 4\lambda_c$ sample

Transient simulations with $L = 4\lambda_c$ revealed both steady-state and traveling-wave solutions for growth rates in the range $0.393\,215 \leq P \leq 0.395\,500$. Simulations leading to both types of solutions involved transients of $\Delta \tau \approx 1000$.

1. Multiple steady-state cells

The transient simulations that lead to steady-state cellular forms are summarized in Table III according to the value of the growth rate, the initial condition and the apparent wavelength of the steady-state cells. Two different initial conditions were used with $P = 0.293\,215$ to compute steady-state cells with wavelength $\frac{4}{5}\lambda_c$. The first was made by using two pairs of outer facing tusks reflected about $x = 2$, the midpoint of the sample. At short times, $\tau < 3000$, the heights of the cells being to os-

cillate and tip splitting occurs. For long times, $\tau > 8000$ (corresponding to 24 h of growth), five cells persisted, the oscillations in cell amplitude decayed and a stable steady state is reached. This transient is shown by the contours of interface height in Fig. 13 and is very similar to a similar one observed in the same size sample and reflective boundary conditions in BB.

The second initial condition for $P = 0.293\,215$ was made by reflecting about $x = 2.0$ the final state ($\tau = 3 \times 10^4$) for the calculation with $L = 2\lambda_c$ at the same growth rate. The interfacial dynamics observed with this initial state is similar to the evolution described above, although the length of time needed to make the transition to five cells in the sample is somewhat longer. This same initial condition was used in simulations with dimensionless growth rates of 0.393 30, 0.393 40, and 0.3940, as listed in Table III. As described below, these calculations lead to different steady-state solutions and to traveling waves.

The simulations with $P = 0.393\,30$ and $P = 0.393\,40$ both returned to steady-state forms with cellular wavelengths of $\frac{4}{5}\lambda_c$ after several thousand time units; the con-
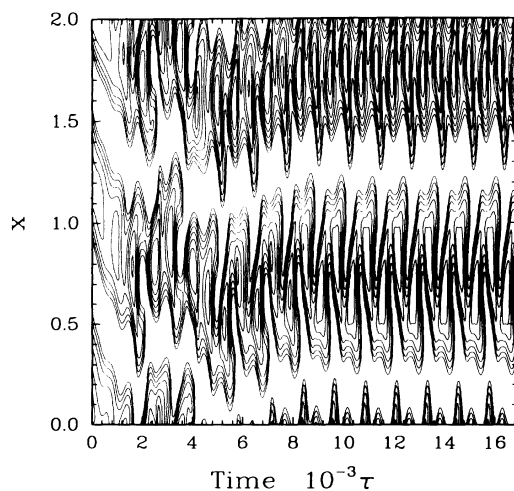

FIG. 12. Contours of interface amplitude for $P = 0.3931$ and $L = 2\lambda_c$. Only contours corresponding to the portion of the interface above the average height are shown.
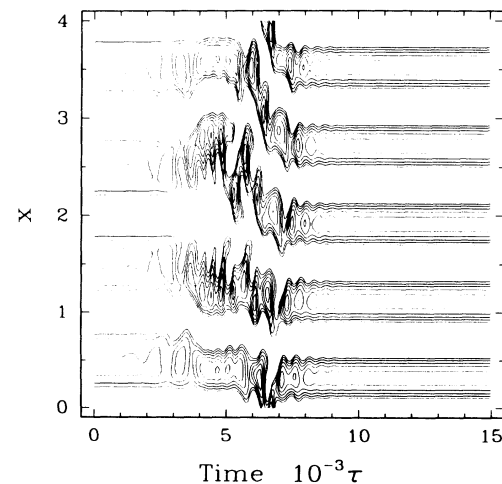

FIG. 13. Contours of interface amplitude for $P = 0.393\,215$ and $L = 4\lambda_c$ started with the second boundary condition listed in Table III.
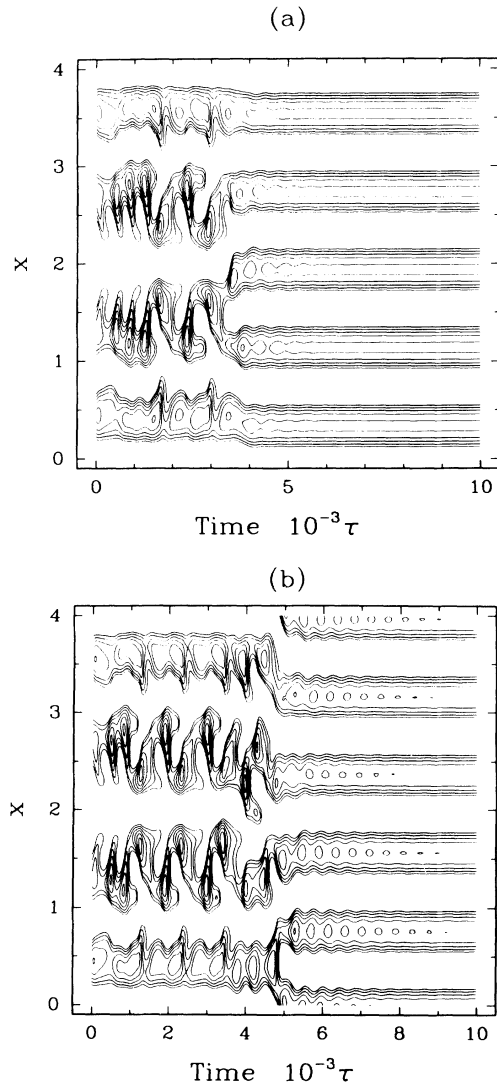
(a)

(b)

FIG. 14. Evolution of interface amplitude with time for simulations listed in Table III with $L=4\lambda_c$ and growth rates of (a) $P=0.3933$ and (b) $P=0.3934$.
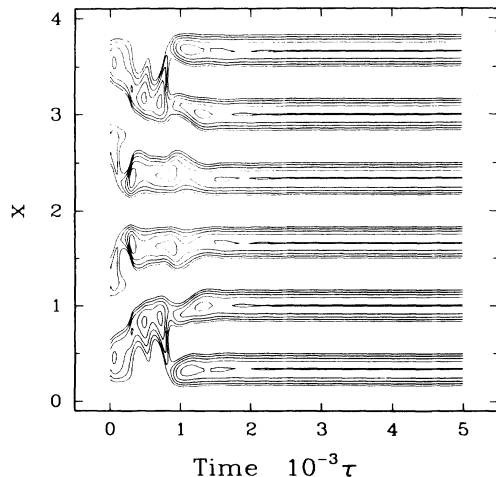

FIG. 15. Contours of interface amplitude for $P=0.3940$ and $L=4\lambda_c$ started with the initial condition listed in Table III.

tours of interface amplitude for these simulations are shown in Fig. 14. The simulation for the highest growth rate, $P=0.3940$, evolved much more quickly to a stable steady-state of cells with wavelength $\frac{2}{3}\lambda_c$. The rolls of tip splitting and lateral motion of the cells are obvious from the contours of interface amplitude shown in Fig. 15.

2. Traveling-wave states

Both stationary and traveling-wave states were identified in simulations for $P=0.393\,50$. Starting a calculation with two pairs of outside facing tusks lead to a long transient involving tip splitting, lateral cell motion, and cell death until the front stabilized with five cells in the sample, $l=\frac{4}{5}\lambda_c$. Traveling-wave states were found using an initial condition composed for four tusk shapes all oriented in the negative x direction. The evolution of the interface amplitude for this simulation is shown in Fig. 16. After only $\Delta\tau\approx 1000$ the front is composed of alternating tusk-shaped and more rounded cells, similar to those seen in the traveling wave solutions for $L=2\lambda_c$ and shown in Fig. 17(b). The initial interface shape and the traveling waves that result at $\tau=1000$ are shown in Fig. 17.

The effect of increasing the growth rate on the form and lateral velocity of the traveling-wave forms was studied in a simulation started with $P=0.3935$ and where P was increased by 5×10^{-4} every 5000 time units. The simulation was initiated with the mirror image of the cells shown in Fig. 17(a), so that the cell travels in the direction of positive x. Increasing the growth rate leads to deep cells and to a faster rate of lateral migration. The increasing deformation of the cells is visible from the evolution of the scaled arc length of the interface with time, which is shown as Fig. 18. Also, the decay of oscillations of the interface shape caused by the step increase in the growth rate is obvious. As in the simulation de-
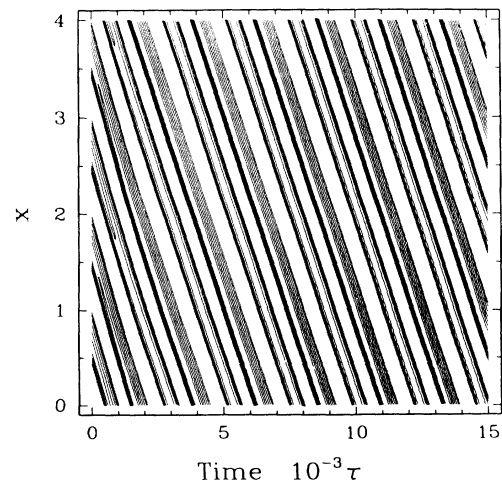

FIG. 16. Contours of interface amplitude for traveling-wave states computed for $L=4\lambda_c$ and $P=0.3935$. Only solid contours representing the portion of the interface with elevations above the mean are shown. Sample interface shapes are shown in Fig. 16.
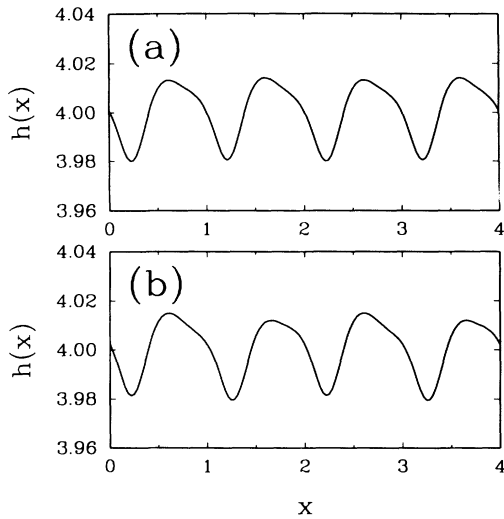
FIG. 17. Sample interface shapes for traveling-wave forms portrayed in Fig. 15 for $P = 0.3935$; (a) $\tau = 0$ and (b) $\tau = 1000$.

FIG. 19. Contours of interface amplitude computed for the simulation shown in Fig. 17. Only solid contours representing the portion of the interface with elevations above the mean are shown.

scribed above for $P = 0.3935$, the interface evolved from four identical tusk-shaped cells to tusks alternated with more rounded forms. This feature of the front persisted until $P = 0.3945$, where in the first 1000 time units of the simulation at this growth rate the front evolved to four identical, tusk-shaped cells. This form continued for the remainder of the calculations at higher growth rates.

The length of the transient needed to reach the new traveling-wave solution after a step in growth rate increased with increasing P, until at $P = 0.3955$, the transient consumed the entire increment of 5000 time units. These oscillations barely damped out, indicating the presence of a pair of complex conjugate eigenvalues with a small negative real part to the linear stability problem for the traveling waves. Further increases in the growth rate

may uncover the mode of instability of these forms. Unfortunately, these calculations could not be pursued here because of the extreme deformation of the interface that results.

The evolution of the contours of the interface amplitude with increasing growth rate is shown in Fig. 19. The increasing slant of the cells corresponds to their increasing translational speed. This dimensionless speed is plotted as a function of the growth rate in Fig. 20 for simulations leading to fronts of like cells and to the alternating
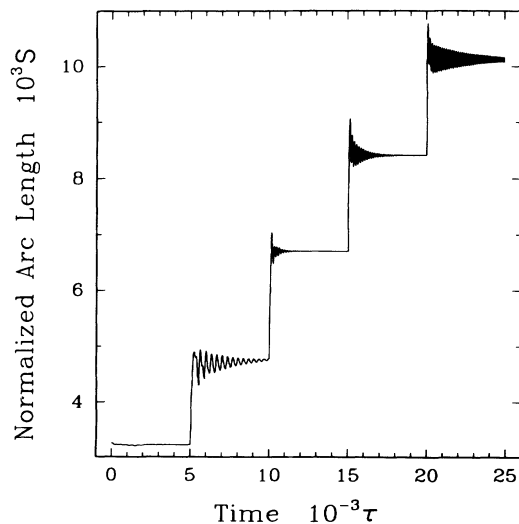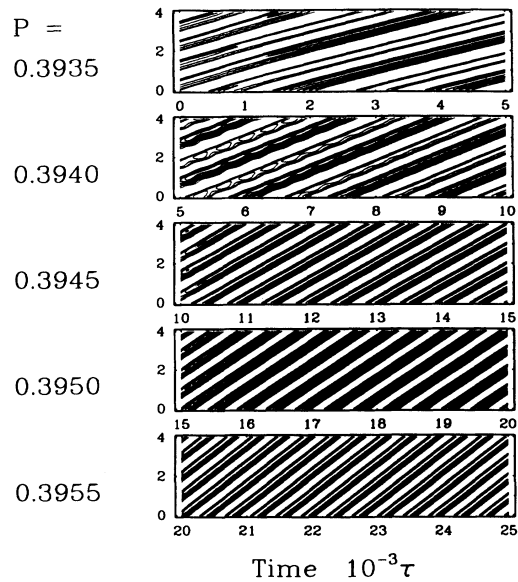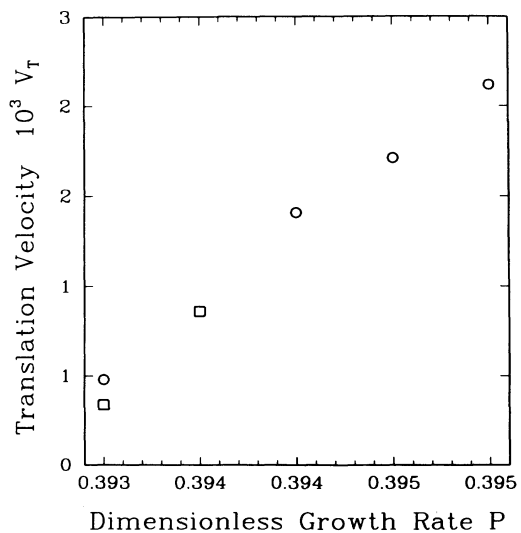

FIG. 18. Evolution of the interfacial arc length as a function of time for simulation with increasing growth rate every 5000 time units. Contours of the interface amplitude are shown in Fig. 13.

FIG. 20. Dependence of dimensionless lateral speed of traveling-wave state on growth rate computed with $L = 4\lambda_c$. Results are shown for traveling waves composed of four nearly identical tusklike cells (circles) and for alternating tusklike and more rounded cells (squares).
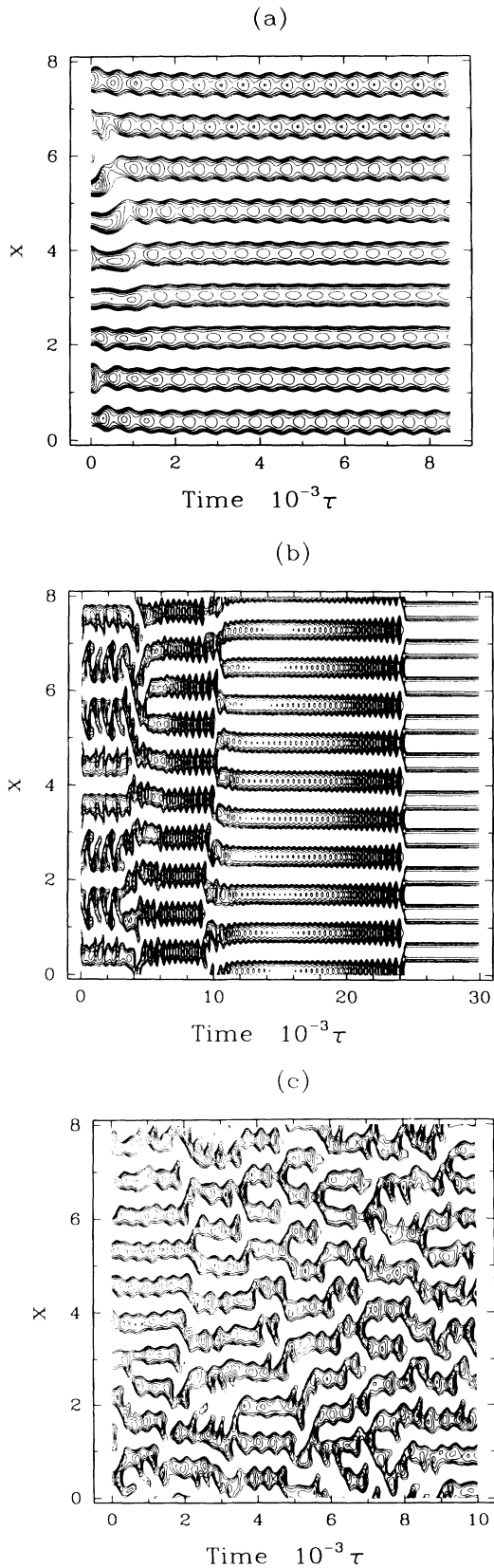
(a)

(b)

(c)

FIG. 21. Contours of interface amplitude for simulations with $L = 8\lambda_c$ and growth rates of (a) 0.3930, (b) 0.3935, and (c) 0.3940. Only solid contours representing the portion of the interface with elevations above the mean are shown.

forms described above. The translation rate is approximately linear with P, as expected from the theory in Refs. 15 and 16.

D. The $L = 8\lambda_c$ sample

The complicated dynamics and long transients seen in the simulations with $L = 4\lambda_c$, compared with the much simpler results in the smaller samples, suggest that simulations with even larger samples will be slower to reach stationary or traveling-wave states. We have attempted four calculations in a sample with $L = 8\lambda_c$ to test this hypothesis. Unfortunately, the large computational expense of these simulations makes these results far from comprehensive and only trends are suggested of the effect of increasing sample size on the simulations.

Three simulations are discussed here for growth rates of 0.3930, 0.3935, and 0.3940. The simulation with $P = 0.3935$ was initiated with the same initial condition described above for the simulation with $L = 4\lambda$ and $P = 0.3935$, but reflected about $x = 4.0$ to create a solution for the larger sample. The contours of the interface amplitude for this simulation are shown as Fig. 21(b). Although a steady-state interface shape with ten cells was reached, corresponding to a wavelength of $\frac{4}{5}\lambda_c$, this did not occur until over 2×10^4 time units. In dimensional terms, the transient lasted three days and required one meter of solidification. It is interesting that ten cells formed after only $\Delta\tau = 5000$, but that the first cells were unstable to amplitude oscillations that lead to tip splitting of several of the cells, the death of others and to an apparent phase shift in the front at $\Delta\tau = 10\,000$. This shifting occurred a second time at $\Delta\tau = 24\,000$ before the steady-state forms results. The growth of the tip oscillations and the abrupt transition to cells with a slight shift in phase is portrayed in Fig. 22(b) by the plot of the interfacial arc length as a function of time. Clearly, there are only small differences in cellular fronts that are stable and those that are unstable to amplitude oscillations and tip splitting.

Simulations at $P = 0.3030$ and $P = 0.3940$ were performed using the solution at $P = 0.3935$ and $\tau = 5000$ as the initial state. Decreasing the growth rate to $P = 0.3930$ damps the amplitude oscillations of the cells and prevents the tip splitting instability; these trends are shown in Figs. 21(a) and 22(a) for the contours of interface amplitude and the arc length, respectively. After an initial transient ($\Delta\tau = 5000$) in which one of the cells is lost, the nine remaining cells begin amplitude oscillations that are essentially periodic. It is interesting to note that the amplitude oscillations of neighboring cells are out of phase. This oscillation pattern is only possible because of the odd number of cells in the sample; by comparison the amplitude oscillations computed for $P = 0.3935$ [see Fig. 21(b)] are approximately in phase. The magnitudes of the oscillations are not uniform along the front, but are strongest for the pair of cells with centers at $x = 6.4$ and 7.5. The amplitude of the deformation decreases with distance along the front from these cells; the cell with center $x = 3.0$ shows the smallest perturbations.

The results of the simulation with $P = 0.3940$ are de-

picted in Figs. 21(c) and 22(c) and show an apparently aperiodic trajectory. The interface contours in Fig. 21(c) reveal many instances of cell splitting and lateral cell motion; however, the perturbations in interface amplitude do not continue across the entire sample, as is true for traveling wave solutions, but instead decay and eventually disappear. The decay length for these disturbances seems to be in the interval $5 \leq \Delta x \leq 8$.

IV. DISCUSSION

This numerical study was undertaken to understand the effect on the dynamics of cellular fronts with large aspect ratio, modeled here by a section of a spatially periodic front, instead of the reflectively symmetric conditions used by BB. The simulations demonstrate two essential characteristics. First, new traveling-wave forms are admissible in the context of an infinite array of periodic cells. This is not surprising in the context of the solution of nonlinear transport problems with periodic boundary conditions, e.g., see Ref. 9, and has been recently discussed in the context of directional solidification by others.[18] Second, states that appear to be spatially and temporally chaotic also are observed when large collections (up to eight) of cells are considered.

Traveling-wave solutions were found in computations with $L = \lambda_c$, $L = 2\lambda_c$, and $L = 4\lambda_c$ for a range of growth rate P. We expect that similar states exist in larger computational domains, e.g., $L = 8\lambda_c$, but that these states
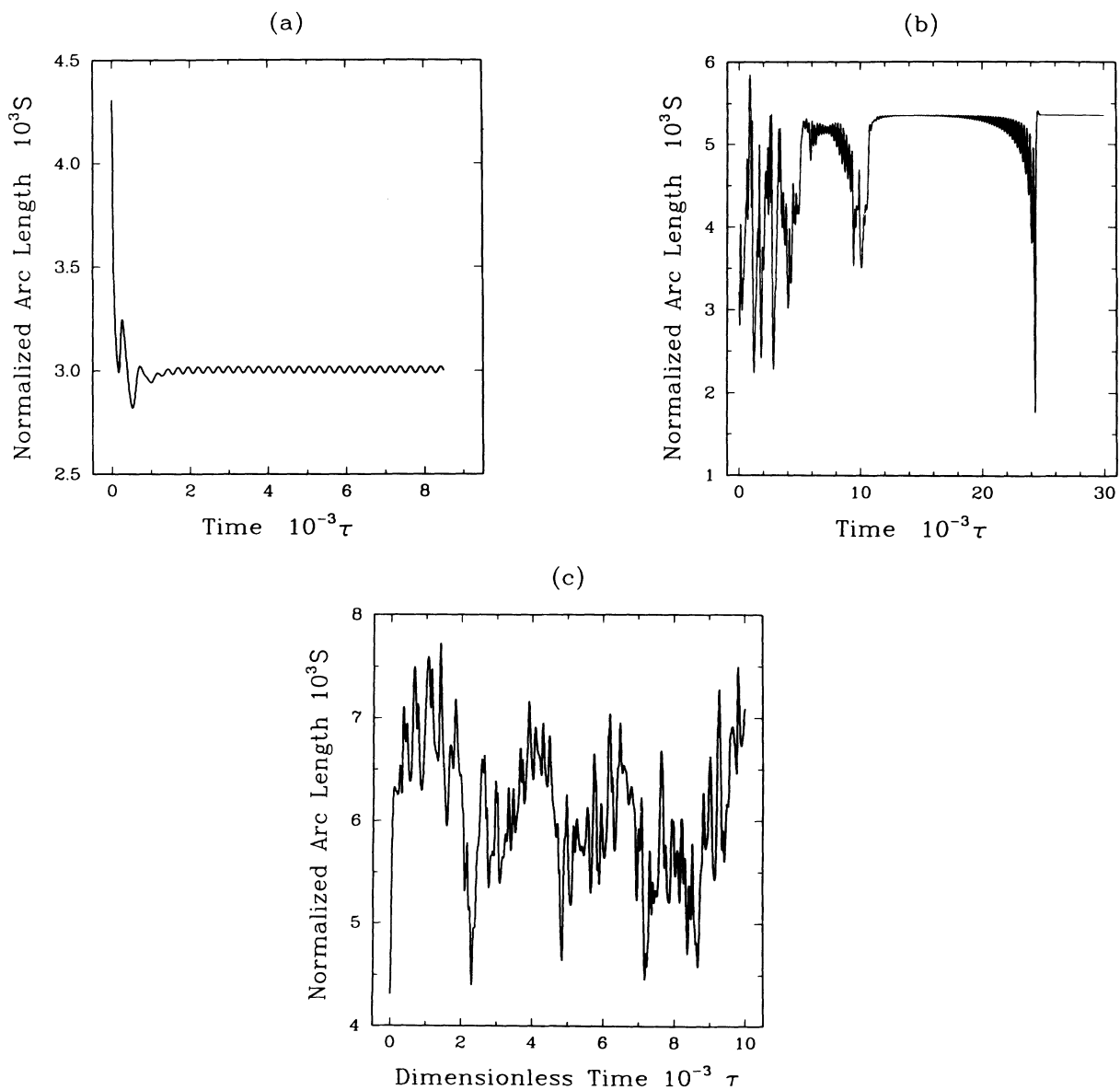

FIG. 22. Evolution of interfacial arc length with time for simulations with $L = 8\lambda_c$ and growth rates of (a) 0.3930, (b) 0.3935, and (c) 0.3940.

may become unstable to perturbations that lead to variations in the cell amplitude and lateral speed. More calculations may lead to the solitonlike cells that move through the front, as described by Simon, Bechhoefer, and Libchaber.[11]

The presence of the traveling-wave states in the calculations with periodic boundaries may explain the complex dynamics observed with reflectively symmetric conditions for $L = 2\lambda_c$ in BB. When placed in a system with reflective boundary conditions, the traveling waves in the cellular front are reflected backwards and collide to produce nonlinear interactions. This scenario for the qualitative difference between the dynamics in small systems with reflective and periodic boundaries was first established by Knobloch and colleagues in studies of time-periodic thermosolutal convection with both types of boundary conditions.[21-23]

The simulations reported here confirm the complex dynamics predicted in BB for small-scale solidification systems. As the size of the system is increased so is the variety of transient behavior observed, including approach to stable steady solutions, stationary time-periodic states, traveling cellular forms, and spatiotemporally chaotic interfaces. However complicated, three interfacial processes seem to be responsible for all the dynamics on the local scale; amplitude oscillation, tip splitting, and cell death or dissolution. The latter two mechanisms have been observed in several experiments,[6,12,24] but amplitude oscillations have not. A possible explanation for this discrepancy is that amplitude oscillations are seen in the simulations only for conditions where a steady-state solution is slightly unstable. This criterion is not typically met in experiments where the large aspect ratios of the cells (depth to wavelength) indicate that the growth rate is substantially above the critical value.

The simulations with periodic boundary conditions substantiate the conclusion in BB that cells with the critical wavelength λ_c are essentially unobservable experimentally. Steady-state calculations in BB predicted that cells with this wavelength were observable only for

$\Delta V = 0.03$ μm/s above the critical value, where a tip splitting instability reduced the wavelength to $\lambda_c / 2$. Simulations with periodic boundary conditions gave stable cells with wavelength λ_c only up to $P = 0.3020$, or 0.15% above critical. Beyond this value new steady-state solutions or time-dependent trajectories lead to cellular structures with lower apparent wavelengths. The wavelength decreased with increasing P. For example, simulations with $L = 8\lambda_c$ predicted steady-state forms with wavelengths or $\frac{8}{9}\lambda_c$ for $P = 0.3930$, $\frac{4}{5}\lambda_c$ for $P = 0.3935$, and time-dependent interface with average wavelength of $\frac{4}{5}\lambda_c$ for $P = 0.3940$. The trend of decreasing wavelength with increasing P agrees with simulations in BB and with experimental data of Eshelman, Seetharaman, and Trivedi.[24] Unfortunately, a qualitative comparison is not feasible because the simulations do not yet cover a wide enough range of growth rate.

Each of the basic dynamical mechanisms—amplitude oscillations, cell splitting, and cell death—occur on relatively long time scales of $O(10^3)$ diffusion time units, as scaled with the wavelength of the cell. We believe that the time scale for these events and the resulting long time scale dynamics of the entire cellular front is a result of the basic mechanism for resonant interactions of neighboring cells that leads to codimension-2 bifurcation behavior and time-periodic dynamics. Analysis for simple models for nonlinear diffusive processes show that the temporal period of these solutions scales as a power of the inverse distance between the critical points for the interacting modes.[25] Hence, the flatness of the neutral stability curve is responsible for the very slow dynamics in the system.

[1]W. W. Mullins and R. F. Sekerka, J. Appl. Phys. **34**, 444 (1964).

[2]L. H. Ungar and R. A. Brown, Phys. Rev. B **29**, 1367 (1984).

[3]N. Ramprasad, M. J. Bennett, and R. A. Brown, Phys. Rev. B **38**, 583 (1988).

[4]R. A. Brown, N. Ramprasad, and M. J. Bennett, in *Supercomputer Research in Chemistry and Chemical Engineering*, ACS Symposium Series, edited by D. G. Truhlar and K. F. Jensen (ACS, Washington, 1987), pp. 295–333.

[5]M. J. Bennett and R. A. Brown, Phys. Rev. B **39**, 11 705 (1989).

[6]T. C. Lee, Ph.D. thesis, Massachusetts Institute of Technology, 1991.

[7]P. Haug, Phys. Rev. A **35**, 2733 (1987).

[8]H. S. Greenside, M. C. Cross, and W. M. Coughan, Jr., Phys. Rev. Lett. **60**, 2269 (1988).

[9]Y. Kuramoto, Prog. Theor. Phys. **71**, 1182 (1984).

[10]M. Rabaud, S. Michalland, and Y. Couder, Phys. Rev. Lett. **64**, 184 (1990).

[11]A. J. Simon, J. Bechhoefer, and A. Libchaber, Phys. Rev. Lett. **61**, 2574 (1988).

[12]P. E. Cladis, J. T. Gleason, and P. L. Finn, in *Defects, Patterns, and Instabilities*, edited by D. Walgref (Kuwer Academic, New York, 1990)

[13]P. E. Cladis, J. T. Gleason, and P. L. Finn (unpublished).

[14]V. Hakim, M. Rabaud, H. Thom, and Y. Couder (unpublished).

[15]P. Coullet, R. E. Goldstein, and G. H. Gunaratne, Phys. Rev. Lett. **63**, 1954 (1989).

[16]R. E. Goldstein, G. H. Gunaratne, L. Gil, and P. Coullet (unpublished).

[17]M. R. E. Proctor and C. A. Jones, J. Fluid Mech. **188**, 301 (1988).

[18]H. Levine and W.-J. Rappel, Phys. Rev. A **42**, 7475 (1990).

[19]L. H. Ungar, N. Ramprasad, and R. A. Brown, J. Sci. Comput. **3**, 77 (1988).

[20]M. J. Bennett, Ph.D. thesis, Massachussetts Institute of Tech-

nology, 1990.

[21]D. R. Moore, J. Toomre, E. Knobloch, and N. O. Weiss, Nature (London) **303**, 663 (1983).

[22]E. Knobloch, D. R. Moore, J. Toomre, and N. O. Weiss, J. Fluid Mech. **166**, 409 (1986).

[23]A. E. Deane, E. Knobloch, and J. Toomre, Phys. Rev. A **37**, 1817 (1988).

[24]M. A. Eshelman, V. Seetharaman, and R. Trivedi, Acta Metall. **36**, 1165 (1988).

[25]K. Tsiveriotis and R. A. Brown (unpublished).